micromachines

MDPI

Article

Bloch Surface Waves in open Fabry-Perot microcavities

Niccolò Marcucci [1], Tianlong Guo [2], Ségolène Pelisset [2], Matthieu Roussey [2], Thierry Grosjean [3] and Emiliano Descrovi [1,*]

[1] Dipartimento di Scienza Applicata e Tecnologia, Politecnico di Torino, 10129 Torino, Italy
[2] Institute of Photonics, Department of Physics and Mathematics, University of Eastern Finland, 80101 Joensuu, Finland
[3] FEMTO-ST Institute, Department of Optics, UMR CNRS 6174, 25030 Besançon, France
* Correspondence: emiliano.descrovi@polito.it

Abstract: Thanks to the increasing availability of technologies for thin film deposition, all-dielectric structures are becoming more and more attractive for integrated photonics. As light-matter interactions are involved, Bloch Surface Waves (BSW) may represent a viable alternative to plasmonic platforms, allowing easy wavelength and polarization manipulation and reduced absorption losses. However, plasmon-based devices operating at optical and near-infrared frequency have demonstrated to reach extraordinary field confinement capabilities, with localized mode volumes down to few nm^3. Although such levels of energy localization are substantially unattainable with dielectrics, it is possible to operate subwavelength field confinement by employing high-refractive index materials with proper patterning as, e.g. photonic crystals and metasurfaces. Here we propose a computational study on the transverse localization of BSW by means of quasi-flat Fabry-Perot microcavities, which have the advantage of being fully exposed toward the outer environment. These structures are constituted by defected periodic corrugations of a dielectric multilayer top surface. The dispersion and spatial distribution of BSW cavity mode are presented. In addition, the hybridization of BSW with the A exciton in a 2D flake of tungsten disulfide is also addressed. We show evidence of strong-coupling involving not only propagating BSW but also localized BSW, namely band-edge and cavity modes.

Keywords: Bloch Surface Waves; strong coupling; TMD; 2D materials

Citation: To be added by editorial staff during production.

Academic Editor: Firstname Lastname

Received: date
Accepted: date
Published: date

1. Introduction

The existence of optical modes strongly confined at the truncation interface of planar dielectric multilayers (one-dimensional Photonic Crystals, -1DPC) is known since decades, from the pioneering studies by P. Yeh and A.Yariv[1,2] and several later works.[3–5] With the advent of the Plasmonics era, the interest toward optical surface modes on planar dielectric stacks has seen a significant boost, mainly thanks to the possibility to overcome some inherent limitations of surface plasmons, especially in sensing applications.[6–9] In the last 20 years, optical surface modes (hereafter called Bloch Surface Waves -BSW) on flat and patterned dielectric multilayers have been investigated in many frameworks, such as strong light-matter coupling,[10–13] integrated,[14–18] guided,[19–22] and fiber[23,24] optics, label-free[25–28] and fluorescence-based[29–31] sensing, metrology,[32] photon management[33–36], light-driven particle manipulation,[37,38] emitting devices[39,40] , microscopy imaging and spectroscopy.[41–43]

Beside the advantages in tuning the BSW spectral position, polarization[44] as well as propagation and penetration lengths[45], one of the most intriguing features offered by 1DPC-based platforms is the possibility to exploit the 1DPC surface for setting up an accessible framework for controlling light-matter interaction. Furthermore, shallow patterning of the 1DPC surface allow the BSW to be manipulated and possibly confined along transverse directions, [40,46] thus providing new degrees of freedom for exploring complex

phenomena. Having a photonic mode confined both out-of-plane and in-plane on a surface is advantageous to alleviate some difficulties in technological tasks such as the integration of emitters/absorbers, which are typically buried/grown within the photonic structure itself, where the radiation energy of photonic modes is generally localized.

In this article we present a computational work describing some peculiar features of TE-polarized BSW confined within linear resonant structures recalling Fabry-Perot microcavities. In addition, the interaction of cavity BSW with the A exciton in a WS_2 monolayer laying on top of the multilayered structure is investigated and discussed. We anticipate strong coupling effects between the BSW cavity mode and the tungsten disulfide (WS_2) A exciton at 2.03 eV, on flakes down to less than 2 μm in transverse size.

2. Computational model

The exemplary model for the 1D photonic crystal considered in this work is constituted by a stack of 5 alternating pairs of TiO_2 and SiO_2 layers on a semi-infinite glass half-space (refractive index $n_{glass} = 1.5$). The TiO_2 and SiO_2 layers have thickness 85 nm and 110 nm respectively. On top of the stack, an additional pair of SiO_2 (90 nm) and TiO_2 (40 nm) layers is introduced, leading to a total of N_L=12 layers. A linear grating acting as a Distributed Bragg Reflector (DBR) is engraved in the top TiO_2 layer, with a modulation height $h = 25$ nm, period $\Lambda_{DBR} = 275$ nm and fill factor 0.5. Furthermore, a linear defect (hereafter called a "spacer") having a width W is introduced within the DBR. A schematic of the structure is presented in Figure 1(a).

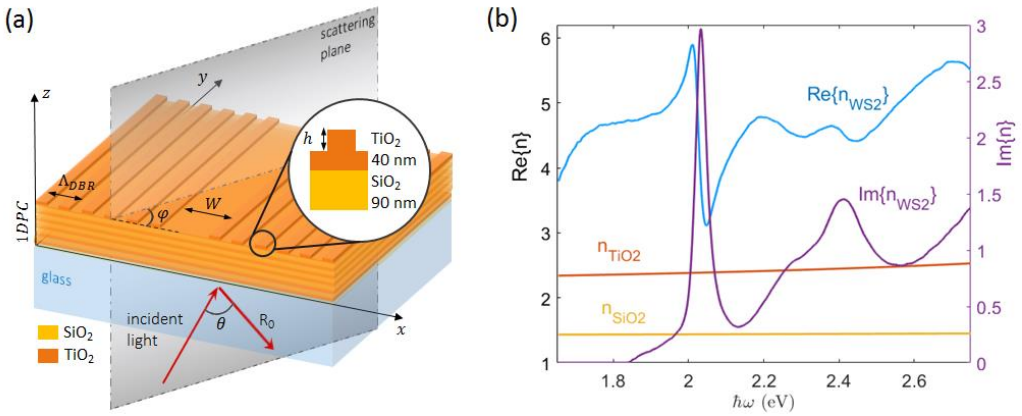

Figure 1. (a) Sketch of the patterned 1DPC in the conical diffraction mounting; (b) refractive index dispersion of the materials employed considered in this work.

This kind of dielectric multilayer can be fabricated by means of standard techniques, including RF sputtering,[16] chemical vapor deposition (CVD) and plasma-enhanced CVD,[47] plasma ion assisted vacuum evaporation (PIAD)[48] and atomic layer deposition (ALD).[49] In particular, the refractive indexes used to design the present stack are taken from ellipsometric data collected on ALD-deposited materials and plotted in Figure 1(b). In addition, the refractive index of a WS_2 monolayer is plotted as well.[50]

Calculations are performed by means of a freely available implementation of the Rigorous Coupled Wave Analysis (RCWA) RETICOLO.[51,52] The RCWA supercell includes the spacer surrounded by 180 DBR periods on each side. The periodic corrugation has an associated Bragg grating vector oriented along the x-axis, i.e. $K_{DBR} = (2\pi \cdot \Lambda_{DBR}^{-1}, 0, 0)$. The conical mounting configuration is considered, so that the incoming radiation can be made incident onto the bottom interface of the multilayer at an incident angle θ with respect to the multilayer normal and at an angle φ with respect to the x-axis. At $\varphi = 0^o$, the incident light is parallel to the K_{DBR} and diffracted accordingly. Illumination is always provided from the glass substrate, in order to reach momentum values beyond the light line in air, as required for BSW coupling. RCWA is a Fourier-based method involving a Rayleigh expansion of the diffracted field as well as a Fourier decomposition of the structure

harmonics. For this reason, it is crucial to define the proper number of Fourier terms to be retained in the calculation. The case of the spacer surrounded by DBRs is addressed with N= 1200 Fourier terms. In the convergence plot in Figure 2, the spectral position of the BSW cavity mode and the corresponding reflectivity are shown as a function of the number of Fourier terms considered. Such a supercell contains a number of DBR periods large enough to avoid significant cross-talk effects between adjacent supercells occurring in the momentum-energy region wherein the cavity mode is located. Instead, the simpler case of a purely periodic corrugation (i.e. no spacer) is modeled as an elementary cell containing a single DBR period and N=60 Fourier terms for assuring reliable results.

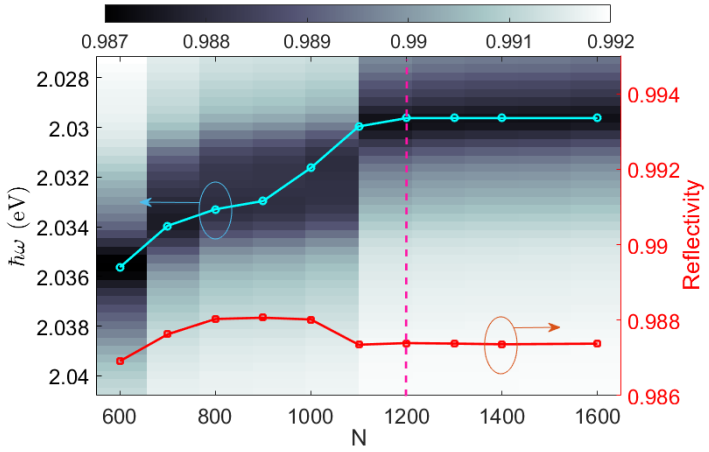

Figure 2. Reflectivity map $R(N, \hbar\omega)$ and spectral position of the BSW resonance (cyan circles) in an exemplary cavity with spacer width $W = 500$ nm and 360 DBR periods overall, at $\varphi = 0^{o}$ incidence. N indicates the number of Fourier terms retained in the RCWA code. The reflectivity values at the resonance center (red squares) are also plotted. The dashed pink line indicates the number of harmonics used in this work.

The multilayer supports TE-polarized Bloch Surface Waves whose dispersion extends from the near-infrared to the visible spectrum. The dispersion of the BSW on the flat multilayer can be inferred upon calculation of the reflectivity $R(\beta, \hbar\omega)$, wherein the effective refractive index is $\beta = n_{\text{glass}} \cdot \sin\theta$ and $\hbar\omega$ is the photon energy of the TE-polarized incident radiation. Without loss of generality, the BSW dispersion can be identified by the pairs $(\beta_{\text{BSW}}, \omega)$ corresponding to the bright line in Figure 3(a). The TiO_2 and SiO_2 layers have been given a small imaginary refractive index $k_{SiO_2} = k_{TiO_2} = 10^{-3}$ in order to introduce enough losses to make the BSW dip well visible on the calculated reflectivity maps. In Figure 3(a,b), the energy- and angularly-resolved map $\log(1 - R)$and the normalized intensity profile of the BSW at $\hbar\omega = 2$ eV are respectively shown.

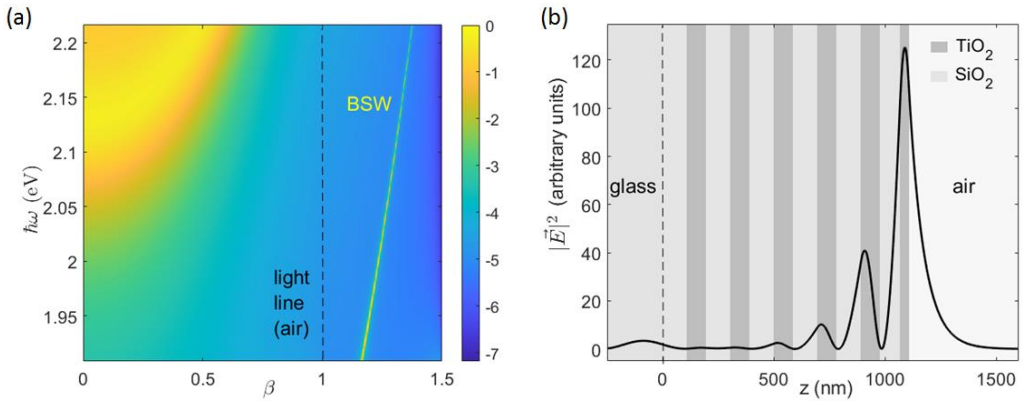

Figure 3. (a) Calculated TE-polarized $\log(1 - R(\beta, \hbar\omega))$ of the flat 1DPC, with illumination from the bottom glass substrate; (b) intensity profile of the BSW at $\hbar\omega = 2$ eV, normalized to the amplitude of the incident wave.

3. Results

The case of the planar stack corrugated with a purely periodic surface modulation (no defect spacer) is considered first. In Figure 4(a), the energy- and angularly-resolved full dispersion of the TE-polarized BSW is shown as a 3D surface whose points $(\beta_x, \beta_y, \omega)$ are extracted from the calculated reflectivity $R(\beta, \varphi, \hbar\omega)$, where $\varphi\epsilon\left[-\frac{\pi}{6}, +\frac{\pi}{6}\right]$. There, $\beta_x = \beta \cdot \cos\varphi$ and $\beta_y = \beta \cdot \sin\varphi$ must match the BSW effective refractive index at any BSW energy $\hbar\omega$, i.e. $\sqrt{\beta_x^2 + \beta_y^2} = \beta_{BSW}(\hbar\omega)$. Reflectivity values $R(\beta, \varphi, \hbar\omega)$ refer to the diffraction efficiency of the 0^{th} order, at different illumination conditions. The periodic modulation along the x-direction results into a folding of the BSW dispersion and the formation of a forbidden band that is dispersed in energy. In order to facilitate the interpretation, the BSW folding and the corresponding energy gap at $\beta_y = 0$ (corresponding to $\varphi = 0$, i.e. a direction parallel to the grating vector K_{DBR}) is presented in Figure 4(b). The folding of the BSW dispersion due to diffraction at the -1^{st} order results into a gap opening at about 2 eV. As pointed out elsewhere,[40,53] the energy gap width depends on the effective refractive index contrast introduced by the periodic modulation. More interestingly, along directions different than K_{DBR}, the gap shifts to higher energies. Band edges are identified at the intersection of the surface $\sigma(\beta_x) = \pi\hbar c \cdot (\Lambda_{DBR} \cdot \beta_x)^{-1}$ (first Brillouin zone boundary, $K_{DBR}/2$) with the full BSW dispersion, as shown in Figure 4(c). The forbidden band can be better appreciated by projecting said BSW dispersion over the σ surface onto the $(\beta_y, \hbar\omega)$ plane (Figure 4(d)). A maximum gap of about 150 meV at $\beta_y = 0$ is found.

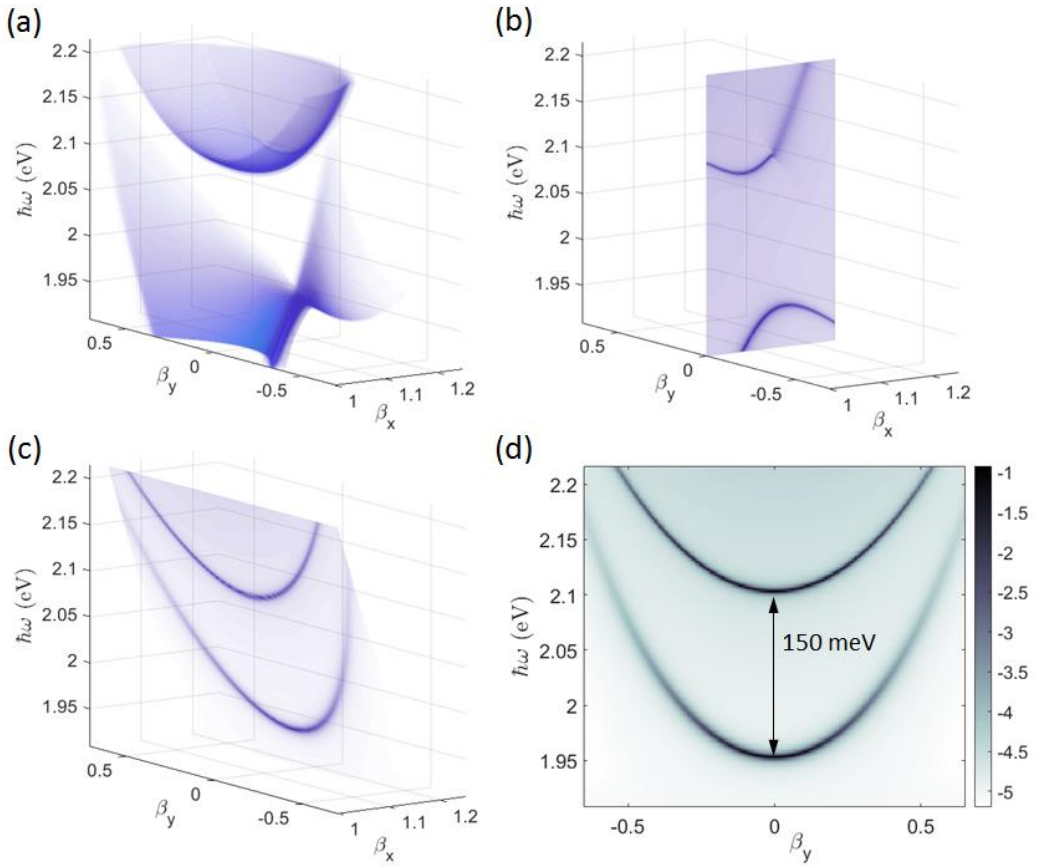

Figure 4. (a) Full dispersion of a TE-polarized BSW represented as a 3D surface from the calculated reflectivity $R(\beta_x, \beta_y, \hbar\omega)$ of the 1DPC patterned with the periodic DBR. Only the region beyond the light-line in air $\sqrt{\beta_x^2 + \beta_y^2} \geq 1$ is considered; BSW dispersion on (b) the $\beta_y = 0$ plane and (c) the boundary of the first Brillouin zone defined by the shaded surface $\sigma = \pi\hbar c \cdot (\Lambda_{DBR} \cdot \beta_x)^{-1}$; (d) $\log\left(1 - R(\beta_x, \beta_y, \hbar\omega)\right)$ map, where $\beta_x = \pi c \cdot (\Lambda_{DBR} \cdot \omega)^{-1}$.

If a linear defect is introduced into the DBR, a cavity mode appears within the forbidden band created by the BSW folding. In Figure 5(a), the BSW cavity mode corresponding to a spacer width $W = 500$ nm is visible as a narrow band starting at about 2.03 eV. In analogy to the spacer mode in a conventional planar microcavity, the BSW cavity mode follows a dispersion curve depending on the momentum component that is transverse to the direction of the refractive index modulation. In our case, since the pattern modulation is developing in the x-direction, the BSW cavity mode is energy-dispersed as a function of β_y. Instead, the BSW cavity mode is dispersionless along the β_x direction (Figure 5(b)).

The spectral position of the cavity mode can be modulated across the forbidden band by varying the spacer width *W* (Figure 5(c)). In Figure 5(d), a cross-sectional view of the spatial near-field intensity of the BSW cavity mode at $\hbar\omega = 2.03$ eV is illustrated. As in a Fabry-Perot planar microcavity, the energy of the cavity mode is preferentially localized in the defect region. However, the very low refractive index contrast experienced by the BSW prevents a strong confinement within the spacer only, with a significant penetration of the mode profile in the surrounding periodic corrugations. The quality factor of the cavity depends weakly on the number N_L of layers in the 1DPC. With the 1DPC design proposed in this work, we estimated a Q factor ranging from Q=340 for N_L=10 to Q= 410 for N_L=16.

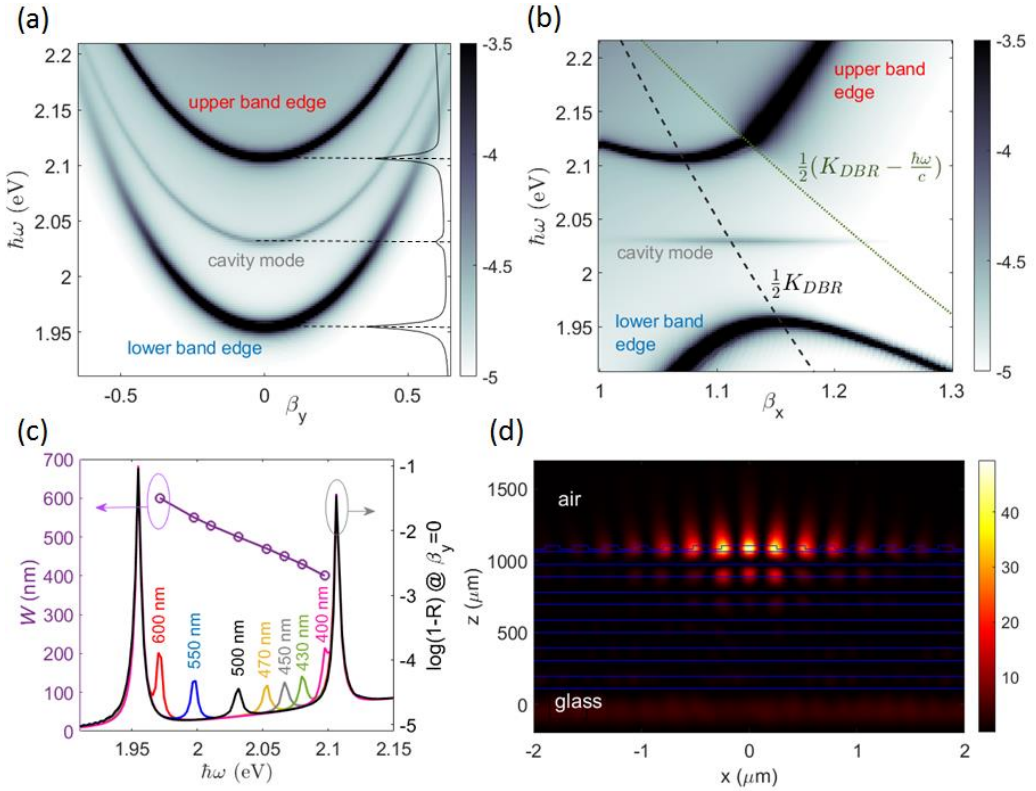

Figure 5. Dispersion of a TE-polarized BSW installed on the 1DPC patterned with a cavity spacer $W = 500$ nm surrounded by 180 DBR periods on each side, calculated on (a) the σ surface, (b) the β_y=0 plane; (c) spectral position of the cavity mode across the forbidden band calculated at $(\beta_x, \beta_y) = (\pi c \cdot (\Lambda_{DBR} \cdot \omega)^{-1}, 0)$ for several spacer values W spanning from 400 nm to 600 nm; (d) near-field intensity of the BSW cavity mode $\langle |E_y(x,z)|^2 \rangle$ for $W = 500$ nm, at $\hbar\omega = 2.032$ eV.

Very recently, multilayers sustaining BSWs coated with organic/inorganic thin layers exhibiting excitonic resonances have been exploited as novel platforms to enhance light-matter interactions.[12,13,54] In this framework, 2D materials (e.g. Transition Metal Dichalcogenides –TMD monolayers) are particularly attractive because of the possibility to operate polariton manipulation at room temperature.[55] Strong coupling effects between BSW

and excitons have been experimentally studied on flat or periodically patterned multilayers, wherein the resulting polariton field exhibits a spatially delocalized distribution. When our flat 1DPC model is coated with a tungsten disulfide (WS_2) monolayer (Figure 6(a)), the BSW dispersion exhibits the typical anti-crossing behavior illustrated in Figure 6(b). The upper and lower BSW polariton branches repel each other by a vacuum Rabi splitting Ω that can be estimated by means of a simple coupled harmonic oscillator model. The system Hamiltonian is a 2x2 matrix with non-zero off-diagonal elements whose eigenvalues are:[12] $E_{up} = {}^1/_2\left(E_{BSW} + E_X + \sqrt{(E_{BSW} - E_X)^2 + \Omega^2}\right)$ and $E_{lp} = {}^1/_2\left(E_{BSW} + E_X - \sqrt{(E_{BSW} - E_X)^2 + \Omega^2}\right)$ for the Upper and the Lower Polariton Branch (UPB and LPB) respectively, where E_X is the exciton energy and $E_{BSW}(\beta_x)$ the dispersion of the uncoupled BSW. A fitting procedure is used to estimate Ω and E_X. Worth to specify that, in order to take into consideration the dielectric loading effect introduced by the WS_2 monolayer, the values for $E_{BSW}(\beta_x)$ calculated for the bare 1DPC need be adjusted (redshift) by an additional energy term E_0 that is also obtained from the fit. In Figure 6(b), the blue and the red dashed lines represent the lower and the upper polariton dispersion respectively, the yellow line is the exciton energy E_X=2.032 eV and the green line is the uncoupled BSW dispersion, redshift-corrected. From the fit, we obtain a Rabi splitting Ω = 52 meV, which is similar to previously published results on a different BSW platform.[13]

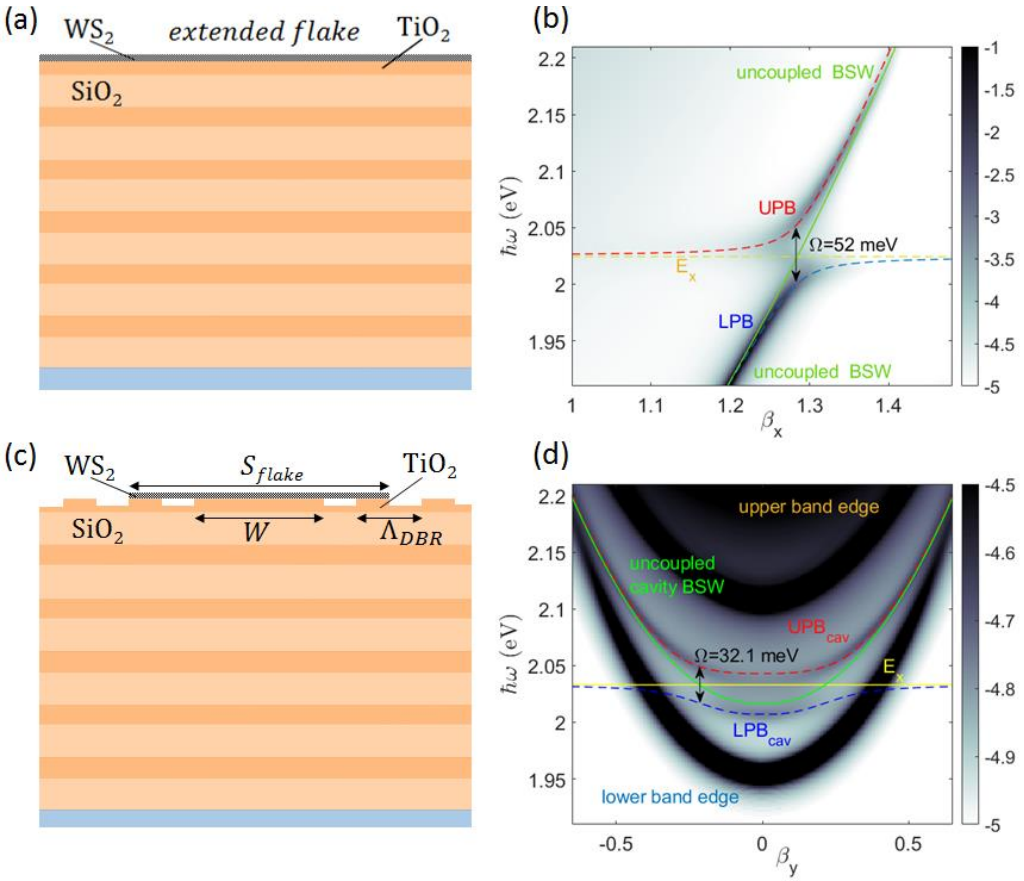

Figure 6. (a) Sketch of the z-cross section of the flat 1DPC topped with a uniform WS_2 monolayer having indefinite extension; (b) corresponding dispersion of BSW polariton; (c) Sketch of the z-cross section of the 1DPC patterned with the cavity topped with a WS_2 monolayer. The flake has a lateral size $S_{flake} = 1.6\ \mu m$ and a thickness 0.65 nm; (d) corresponding dispersion of the BSW cavity-polariton branches (UPB_{cav} and LPB_{cav}).

When the BSW cavity is considered, the BSW-exciton interaction occurs over a spatial region limited to the transverse size of the cavity mode. The sketch in Figure 6(c) shows the case of a WS_2 monolayer deposited on top of the BSW cavity, extending over the spacer and the first surrounding DBR period, with a total size $S_{flake} = 1.6\ \mu m$ and a thickness of

0.65 nm.[56] Similarly to cavity modes in planar microcavity, here the BSW hybridize with the excitonic resonance, resulting in a mode dispersion splitting into an upper and a lower polariton branches (UPB_{cav} and LPB_{cav}), as shown in Figure 6(d). The Rabi splitting estimated with the fitting procedure described above is found to be $\Omega = 32.1$ meV. Given the half-widths of the BSW cavity mode γ_{BSW} =6 meV and the A exciton of WS_2 γ_X =11 meV,[57,58] the condition for the occurrence of strong coupling. i.e. $\Omega > \frac{1}{2}(\gamma_{BSW} + \gamma_X)$, is fulfilled.

It is interesting to note that the BSW hybridization presented above involves the cavity mode only. This is due to the limited size of the WS_2 monolayer, which overlaps mainly with the cavity spacer, wherein most of the energy is localized. Instead, if the whole patterned 1DPC is topped with an extended monolayer (Figure 7(a)), the BSW hybridization is found to occur also with the BSW band edge modes, as shown in Figure 7(b,c), resulting into an upper and a lower band edge-polariton branches (UPB_{be} and LPB_{be}). Here, we find a Rabi splitting $\Omega = 37$ meV for the BSW cavity polariton, and $\Omega = 37.6$ meV for the lower BSW band edge polariton. The different spatial distribution of the band edge and the cavity modes enables to further modulate the photonic mode-exciton interaction, by controlling size and position of the WS_2 monolayer on the BSW platform.

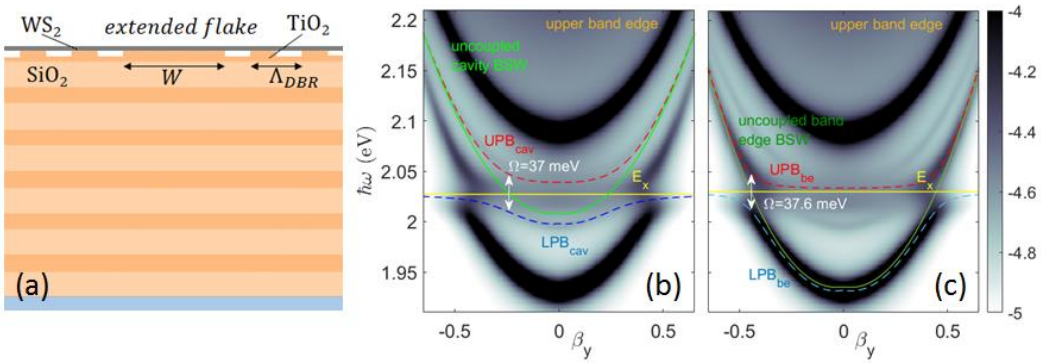

Figure 7. (a) Sketch of the z-cross section of the 1DPC patterned with the cavity topped with an indefinitely large WS_2 monolayer; corresponding dispersions of hybridized (b) BSW cavity-polariton mode UPB_{cav}, LPB_{cav} and (c) BSW band edge-polariton mode UPB_{be}, LPB_{be}.

4. Discussion

Fostered by an increasing interest toward surface waves on dielectric photonic platforms, we investigated some aspects of transverse confinement of BSW in quasi-flat Fabry-Perot microcavities. Despite the low effective refractive index contrast produced by ultra-shallow patterning/modulations of the multilayer surface, BSWs can be made resonantly confined within sub-micrometric regions. As an extension of the findings presented here, an omnidirectional confinement on the multilayer plane can be obtained by introducing axis-symmetric corrugations[40] or dielectric ridges.[46] The design of the surface modulation should be addressed in conjunction with the multilayer design, as dielectric loading/unloading effects can significantly affect the BSW dispersion, resulting in momentum mismatch with the pattern. In the exemplary cases presented here, we designed Fabry-Perot cavities having Q factors ranging from 340 to 410 by employing materials and geometries that can be realistically handled for device fabrication. When considering the in-plane momentum transverse to the grating vector, we found the cavity mode following a parabolic energy dispersion similar to stacked 3D planar microcavities.

One of the main advantages in BSW-based platforms is the possibility of enhancing light-matter interaction on the surface of the photonic structure. This aspect is particularly useful in the framework of 2D materials such as TMD, that are often transferred on planar or structured surfaces upon exfoliation from bulk. We addressed the hybridization of a BSW cavity mode with the A exciton in a WS_2 monolayer deposited thereto. Strong coupling is found with both the cavity and the band-edge modes, depending on the spatial

overlap with the interacting modal volumes, resulting into vacuum Rabi splitting in the range from 30 meV and 40 meV.

Our findings contribute to advancing knowledge on BSW-based platforms, in particular on polariton control at room temperature. We anticipate future opportunities for embedding TMDs on dielectric multilayers, in the perspective of integrated quantum nanophotonic devices.[59]

Author Contributions: N.M. has set up the computational model and run the calculations; Ti.Gu. has performed deposition of TiO_2 and SiO_2 layers, S.P. and M.R. have conducted ellipsometric measurements and fitting procedures for the refractive index estimation; Th.Gr. has provided the BSW cavity design; E.D. has coordinated the work. All authors have contributed to writing the manuscript. All authors have read and agreed to the published version of the manuscript.

Funding: This research was partially funded by the "Dipartimento di Eccellenza 2018-2022" program from the Italian Ministry of Education, University and Research.

Data Availability Statement: Not applicable.

Acknowledgments: Computational resources were provided by HPC@POLITO, a project of Academic Computing within the Department of Control and Computer Engineering at the Politecnico di Torino (http://hpc.polito.it)

Conflicts of Interest: The authors declare no conflict of interest. The funders had no role in the design of the study; in the collection, analyses, or interpretation of data; in the writing of the manuscript; or in the decision to publish the results.

References

(1) Yeh, P.; Yariv, A.; Hong, C.-S. Electromagnetic Propagation in Periodic Stratified Media I General Theory*. *J. Opt. Soc. Am.* **1977**, *67* (4), 423. https://doi.org/10.1364/JOSA.67.000423.

(2) Yeh, P.; Yariv, A.; Cho, A. Y. Optical Surface Waves in Periodic Layered Media. *Appl. Phys. Lett.* **1978**, *32* (2), 104–105. https://doi.org/10.1063/1.89953.

(3) Meade, R. D.; Brommer, K. D.; Rappe, A. M.; Joannopoulos, J. D. Electromagnetic Bloch Waves at the Surface of a Photonic Crystal. *Phys. Rev. B* **1991**, *44* (19), 10961–10964. https://doi.org/10.1103/PhysRevB.44.10961.

(4) Robertson, W. M.; Arjavalingam, G.; Meade, R. D.; Brommer, K. D.; Rappe, A. M.; Joannopoulos, J. D. Observation of Surface Photons on Periodic Dielectric Arrays. *Opt. Lett.* **1993**, *18* (7), 528. https://doi.org/10.1364/OL.18.000528.

(5) Robertson, W. M. Experimental Measurement of the Effect of Termination on Surface Electromagnetic Waves in One-Dimensional Photonic Bandgap Arrays. *J. Lightwave Technol.* **1999**, *17* (11), 2013–2017. https://doi.org/10.1109/50.802988.

(6) Villa, F.; Regalado, L. E.; Ramos-Mendieta, F.; Gaspar-Armenta, J.; Lopez-Ríos, T. Photonic Crystal Sensor Based on Surface Waves for Thin-Film Characterization. *Opt. Lett.* **2002**, *27* (8), 646. https://doi.org/10.1364/OL.27.000646.

(7) Shinn, M.; Robertson, W. M. Surface Plasmon-like Sensor Based on Surface Electromagnetic Waves in a Photonic Band-Gap Material. *Sensors and Actuators B: Chemical* **2005**, *105* (2), 360–364. https://doi.org/10.1016/j.snb.2004.06.024.

(8) Descrovi, E.; Frascella, F.; Sciacca, B.; Geobaldo, F.; Dominici, L.; Michelotti, F. Coupling of Surface Waves in Highly Defined One-Dimensional Porous Silicon Photonic Crystals for Gas Sensing Applications. *Appl. Phys. Lett.* **2007**, *91* (24), 241109. https://doi.org/10.1063/1.2824387.

(9) Liscidini, M.; Sipe, J. E. Enhancement of Diffraction for Biosensing Applications via Bloch Surface Waves. *Appl. Phys. Lett.* **2007**, *91* (25), 253125. https://doi.org/10.1063/1.2826545.

(10) Liscidini, M.; Gerace, D.; Sanvitto, D.; Bajoni, D. Guided Bloch Surface Wave Polaritons. *Appl. Phys. Lett.* **2011**, *98* (12), 121118. https://doi.org/10.1063/1.3571285.

(11) Pirotta, S.; Patrini, M.; Liscidini, M.; Galli, M.; Dacarro, G.; Canazza, G.; Guizzetti, G.; Comoretto, D.; Bajoni, D. Strong Coupling between Excitons in Organic Semiconductors and Bloch Surface Waves. *Appl. Phys. Lett.* **2014**, *104* (5), 051111. https://doi.org/10.1063/1.4863853.

(12) Henn, S.; Grundmann, M.; Sturm, C. Strong Coupling of Bloch Surface Waves and Excitons in ZnO up to 430 K. *New J. Phys.* **2021**, *23* (9), 093031. https://doi.org/10.1088/1367-2630/ac2452.

(13) Lerario, G.; Ballarini, D.; Fieramosca, A.; Cannavale, A.; Genco, A.; Mangione, F.; Gambino, S.; Dominici, L.; De Giorgi, M.; Gigli, G.; Sanvitto, D. High-Speed Flow of Interacting Organic Polaritons. *Light Sci Appl* **2017**, *6* (2), e16212–e16212. https://doi.org/10.1038/lsa.2016.212.

(14) Dubey, R.; Vosoughi Lahijani, B.; Barakat, E.; Häyrinen, M.; Roussey, M.; Kuittinen, M.; Herzig, H. P. Near-Field Characterization of a Bloch-Surface-Wave-Based 2D Disk Resonator. *Opt. Lett.* **2016**, *41* (21), 4867. https://doi.org/10.1364/OL.41.004867.

(15) Rodriguez, G. A.; Aurelio, D.; Liscidini, M.; Weiss, S. M. Bloch Surface Wave Ring Resonator Based on Porous Silicon. *Appl. Phys. Lett.* **2019**, *115* (1), 011101. https://doi.org/10.1063/1.5093435.

(16) Deng, C.-Z.; Ho, Y.-L.; Yamahara, H.; Tabata, H.; Delaunay, J.-J. Near-Zero-Index Slabs on Bloch Surface Wave Platform for Long-Range Directional Couplers and Optical Logic Gates. *ACS Nano* **2022**, *16* (2), 2224–2232. https://doi.org/10.1021/acsnano.1c08318.

(17) Kim, M.-S.; Vosoughi Lahijani, B.; Descharmes, N.; Straubel, J.; Negredo, F.; Rockstuhl, C.; Häyrinen, M.; Kuittinen, M.; Roussey, M.; Herzig, H. P. Subwavelength Focusing of Bloch Surface Waves. *ACS Photonics* **2017**, *4* (6), 1477–1483. https://doi.org/10.1021/acsphotonics.7b00245.

(18) Augenstein, Y.; Roussey, M.; Grosjean, T.; Descrovi, E.; Rockstuhl, C. Inverse Design of Cavities for Bloch Surface Waves Interfaced to Integrated Waveguides. *Photonics and Nanostructures - Fundamentals and Applications* **2022**, 101079. https://doi.org/10.1016/j.photonics.2022.101079.

(19) Descrovi, E.; Sfez, T.; Quaglio, M.; Brunazzo, D.; Dominici, L.; Michelotti, F.; Herzig, H. P.; Martin, O. J. F.; Giorgis, F. Guided Bloch Surface Waves on Ultrathin Polymeric Ridges. *Nano Lett.* **2010**, *10* (6), 2087–2091. https://doi.org/10.1021/nl100481q.

(20) Baghbadorani, H. K.; Aurelio, D.; Barvestani, J.; Liscidini, M. Guided Modes in Photonic Crystal Slabs Supporting Bloch Surface Waves. *J. Opt. Soc. Am. B* **2018**, *35* (4), 805. https://doi.org/10.1364/JOSAB.35.000805.

(21) Yu, L.; Barakat, E.; Sfez, T.; Hvozdara, L.; Di Francesco, J.; Peter Herzig, H. Manipulating Bloch Surface Waves in 2D: A Platform Concept-Based Flat Lens. *Light Sci Appl* **2014**, *3* (1), e124–e124. https://doi.org/10.1038/lsa.2014.5.

(22) Dubey, R.; Barakat, E.; Häyrinen, M.; Roussey, M.; Honkanen, S. K.; Kuittinen, M.; Herzig, H. P. Experimental Investigation of the Propagation Properties of Bloch Surface Waves on Dielectric Multilayer Platform. *J. Eur. Opt. Soc.-Rapid Publ.* **2017**, *13* (1), 5. https://doi.org/10.1186/s41476-016-0029-1.

(23) Scaravilli, M.; Castaldi, G.; Cusano, A.; Galdi, V. Grating-Coupling-Based Excitation of Bloch Surface Waves for Lab-on-Fiber Optrodes. *Opt. Express* **2016**, *24* (24), 27771. https://doi.org/10.1364/OE.24.027771.

(24) Scaravilli, M.; Micco, A.; Castaldi, G.; Coppola, G.; Gioffrè, M.; Iodice, M.; La Ferrara, V.; Galdi, V.; Cusano, A. Excitation of Bloch Surface Waves on an Optical Fiber Tip. *Advanced Optical Materials* **2018**, *6* (19), 1800477. https://doi.org/10.1002/adom.201800477.

(25) Niu, D.; Zerrad, M.; Lereu, A.; Moreau, A.; Lumeau, J.; Zapien, J. A.; Passian, A.; Aubry, V.; Amra, C. Excitation of Bloch Surface Waves in Zero-Admittance Multilayers for High-Sensitivity Sensor Applications. *Phys. Rev. Applied* **2020**, *13* (5), 054064. https://doi.org/10.1103/PhysRevApplied.13.054064.

(26) Occhicone, A.; Polito, R.; Michelotti, F.; Ortolani, M.; Baldassarre, L.; Pea, M.; Sinibaldi, A.; Notargiacomo, A.; Cibella, S.; Mattioli, F.; Roy, P.; Brubach, J.-B.; Calvani, P.; Nucara, A. Low-Temperature Stability and Sensing Performance of Mid-Infrared Bloch Surface Waves on a One-Dimensional Photonic Crystal. *ACS Appl. Mater. Interfaces* **2022**, *14* (38), 43853–43860. https://doi.org/10.1021/acsami.2c07894.

(27) Gryga, M.; Ciprian, D.; Gembalova, L.; Hlubina, P. Sensing Based on Bloch Surface Wave and Self-Referenced Guided Mode Resonances Employing a One-Dimensional Photonic Crystal. *Opt. Express* **2021**, *29* (9), 12996. https://doi.org/10.1364/OE.421162.

(28) Zhang, C.; Liu, Q.; Peng, X.; Ouyang, Z.; Shen, S. Sensitive THz Sensing Based on Fano Resonance in All-Polymeric Bloch Surface Wave Structure. *Nanophotonics* **2021**, *10* (15), 3879–3888. https://doi.org/10.1515/nanoph-2021-0339.

(29) Sinibaldi, A.; Doricchi, A.; Pileri, T.; Allegretti, M.; Danz, N.; Munzert, P.; Giordani, E.; Giacomini, P.; Michelotti, F. Bioassay Engineering: A Combined Label-Free and Fluorescence Approach to Optimize HER2 Detection in Complex Biological Media. *Anal Bioanal Chem* **2020**, *412* (14), 3509–3517. https://doi.org/10.1007/s00216-020-02643-3.

(30) Sinibaldi, A.; Montaño-Machado, V.; Danz, N.; Munzert, P.; Chiavaioli, F.; Michelotti, F.; Mantovani, D. Real-Time Study of the Adsorption and Grafting Process of Biomolecules by Means of Bloch Surface Wave Biosensors. *ACS Appl. Mater. Interfaces* **2018**, *10* (39), 33611–33618. https://doi.org/10.1021/acsami.8b08335.

(31) Bhaskar, S.; Das, P.; Srinivasan, V.; Bhaktha B. N., S.; Ramamurthy, S. S. Bloch Surface Waves and Internal Optical Modes-Driven Photonic Crystal-Coupled Emission Platform for Femtomolar Detection of Aluminum Ions. *J. Phys. Chem. C* **2020**, *124* (13), 7341–7352. https://doi.org/10.1021/acs.jpcc.9b11092.

(32) Wang, R.; Lei, X.; Jin, Y.; Wen, X.; Du, L.; Wu, A.; Yuan, X. Unipolar Excitation of Bloch Surface Waves for Ultrasensitive Displacement Metrology. 20.

(33) Stella, U.; Grosjean, T.; De Leo, N.; Boarino, L.; Munzert, P.; Lakowicz, J. R.; Descrovi, E. Vortex Beam Generation by Spin-Orbit Interaction with Bloch Surface Waves. *ACS Photonics* **2020**, *7* (3), 774–783. https://doi.org/10.1021/acsphotonics.9b01625.

(34) Bezus, E. A.; Bykov, D. A.; Doskolovich, L. L. Integrated Diffraction Gratings on the Bloch Surface Wave Platform Supporting Bound States in the Continuum. *Nanophotonics* **2021**, *10* (17), 4331–4340. https://doi.org/10.1515/nanoph-2021-0352.

(35) Deng, C.-Z.; Ho, Y.-L.; Clark, J. K.; Yatsui, T.; Delaunay, J.-J. Light Switching with a Metal-Free Chiral-Sensitive Metasurface at Telecommunication Wavelengths. *ACS Photonics* **2020**, *7* (10), 2915–2922. https://doi.org/10.1021/acsphotonics.0c01377.

(36) Kovalevich, T.; Belharet, D.; Robert, L.; Kim, M.-S.; Herzig, H. P.; Grosjean, T.; Bernal, M.-P. Experimental Evidence of Bloch Surface Waves on Photonic Crystals with Thin-Film LiNbO_3 as a Top Layer. *Photon. Res.* **2017**, *5* (6), 649. https://doi.org/10.1364/PRJ.5.000649.

(37) Shilkin, D. A.; Lyubin, E. V.; Soboleva, I. V.; Fedyanin, A. A. Direct Measurements of Forces Induced by Bloch Surface Waves in a One-Dimensional Photonic Crystal. *Opt. Lett.* **2015**, *40* (21), 4883. https://doi.org/10.1364/OL.40.004883.

(38) Xiang, Y.; Tang, X.; Fu, Y.; Lu, F.; Kuai, Y.; Min, C.; Chen, J.; Wang, P.; Lakowicz, Joseph. R.; Yuan, X.; Zhang, D. Trapping Metallic Particles Using Focused Bloch Surface Waves. *Nanoscale* **2020**, *12* (3), 1688–1696. https://doi.org/10.1039/C9NR08399E.

(39) Safronov, K. R.; Popkova, A. A.; Markina, D. I.; Pushkarev, A. P.; Makarov, S. V.; Bessonov, V. O.; Fedyanin, A. A. Efficient Emission Outcoupling from Perovskite Lasers into Highly Directional and Long-Propagation-Length Bloch Surface Waves. *Laser & Photonics Reviews* **2022**, *16* (6), 2100728. https://doi.org/10.1002/lpor.202100728.

(40) Stella, U.; Boarino, L.; De Leo, N.; Munzert, P.; Descrovi, E. Enhanced Directional Light Emission Assisted by Resonant Bloch Surface Waves in Circular Cavities. *ACS Photonics* **2019**, *6* (8), 2073–2082. https://doi.org/10.1021/acsphotonics.9b00570.

(41) Pirotta, S.; Xu, X. G.; Delfan, A.; Mysore, S.; Maiti, S.; Dacarro, G.; Patrini, M.; Galli, M.; Guizzetti, G.; Bajoni, D.; Sipe, J. E.; Walker, G. C.; Liscidini, M. Surface-Enhanced Raman Scattering in Purely Dielectric Structures via Bloch Surface Waves. *J. Phys. Chem. C* **2013**, *117* (13), 6821–6825. https://doi.org/10.1021/jp400223f.

(42) Ray, K.; Badugu, R.; Lakowicz, J. R. Bloch Surface Wave-Coupled Emission from Quantum Dots by Ensemble and Single Molecule Spectroscopy. *RSC Adv.* **2015**, *5* (67), 54403–54411. https://doi.org/10.1039/C5RA03413B.

(43) Mouttou, A.; Lemarchand, F.; Koc, C.; Moreau, A.; Lumeau, J.; Favard, C.; Lereu, A. L. Optimization of Resonant Dielectric Multilayer for Enhanced Fluorescence Imaging. *Optical Materials: X* **2022**, 100223. https://doi.org/10.1016/j.omx.2022.100223.

(44) Mogni, E.; Pellegrini, G.; Gil-Rostra, J.; Yubero, F.; Simone, G.; Fossati, S.; Dostálek, J.; Martínez Vázquez, R.; Osellame, R.; Celebrano, M.; Finazzi, M.; Biagioni, P. One-Dimensional Photonic Crystal for Surface Mode Polarization Control. *Advanced Optical Materials* **2022**, *10* (21), 2200759. https://doi.org/10.1002/adom.202200759.

(45) Vosoughi Lahijani, B.; Descharmes, N.; Barbey, R.; Osowiecki, G. D.; Wittwer, V. J.; Razskazovskaya, O.; Südmeyer, T.; Herzig, H. P. Centimeter-Scale Propagation of Optical Surface Waves at Visible Wavelengths. *Advanced Optical Materials* **2022**, *10* (10), 2102854. https://doi.org/10.1002/adom.202102854.

(46) Perani, T.; Aurelio, D.; Liscidini, M. Bloch-Surface-Wave Photonic Crystal Nanobeam Cavity. *Opt. Lett.* **2019**, *44* (21), 5133. https://doi.org/10.1364/OL.44.005133.

(47) Mandracci, P.; Frascella, F.; Rizzo, R.; Virga, A.; Rivolo, P.; Descrovi, E.; Giorgis, F. Optical and Structural Properties of Amorphous Silicon-Nitrides and Silicon-Oxycarbides: Application of Multilayer Structures for the

Coupling of Bloch Surface Waves. *Journal of Non-Crystalline Solids* **2016**, *453*, 113–117. https://doi.org/10.1016/j.jnoncrysol.2016.10.002.

(48) Munzert, P.; Danz, N.; Sinibaldi, A.; Michelotti, F. Multilayer Coatings for Bloch Surface Wave Optical Biosensors. *Surface and Coatings Technology* **2017**, *314*, 79–84. https://doi.org/10.1016/j.surfcoat.2016.08.029.

(49) Kovalevich, T.; Ndao, A.; Suarez, M.; Tumenas, S.; Balevicius, Z.; Ramanavicius, A.; Baleviciute, I.; Häyrinen, M.; Roussey, M.; Kuittinen, M.; Grosjean, T.; Bernal, M.-P. Tunable Bloch Surface Waves in Anisotropic Photonic Crystals Based on Lithium Niobate Thin Films. *Opt. Lett.* **2016**, *41* (23), 5616. https://doi.org/10.1364/OL.41.005616.

(50) Hsu, C.; Frisenda, R.; Schmidt, R.; Arora, A.; de Vasconcellos, S. M.; Bratschitsch, R.; van der Zant, H. S. J.; Castellanos-Gomez, A. Thickness-Dependent Refractive Index of 1L, 2L, and 3L MoS2, MoSe2, WS2, and WSe2. *Advanced Optical Materials* **2019**, *7* (13), 1900239. https://doi.org/10.1002/adom.201900239.

(51) Hugonin, J. P.; Lalanne, P. RETICOLO Software for Grating Analysis. 57. https://doi.org/10.48550.arXiv:2101.00901.

(52) Lalanne, P.; Morris, G. M. Highly Improved Convergence of the Coupled-Wave Method for TM Polarization. *J. Opt. Soc. Am. A* **1996**, *13* (4), 779–784. https://doi.org/10.1364/JOSAA.13.000779.

(53) Sfez, T.; Descrovi, E.; Dominici, L.; Nakagawa, W.; Michelotti, F.; Giorgis, F.; Herzig, H.-P. Near-Field Analysis of Surface Electromagnetic Waves in the Bandgap Region of a Polymeric Grating Written on a One-Dimensional Photonic Crystal. *Appl. Phys. Lett.* **2008**, *93* (6), 061108. https://doi.org/10.1063/1.2970961.

(54) Ardizzone, V.; De Marco, L.; De Giorgi, M.; Dominici, L.; Ballarini, D.; Sanvitto, D. Emerging 2D Materials for Room-Temperature Polaritonics. *Nanophotonics* **2019**, *8* (9), 1547–1558. https://doi.org/10.1515/nanoph-2019-0114.

(55) Lerario, G.; Ballarini, D.; Dominici, L.; Fieramosca, A.; Cannavale, A.; Holwill, M.; Kozikov, A.; Novoselov, K.; Gigli, G. Bloch Surface Waves for MoS2 Emission Coupling and Polariton Systems. *Applied Sciences* **2017**, *7* (12), 1217. https://doi.org/10.3390/app7121217.

(56) Kim, H.-C.; Kim, H.; Lee, J.-U.; Lee, H.-B.; Choi, D.-H.; Lee, J.-H.; Lee, W. H.; Jhang, S. H.; Park, B. H.; Cheong, H.; Lee, S.-W.; Chung, H.-J. Engineering Optical and Electronic Properties of WS_2 by Varying the Number of Layers. *ACS Nano* **2015**, *9* (7), 6854–6860. https://doi.org/10.1021/acsnano.5b01727.

(57) Flatten, L. C.; He, Z.; Coles, D. M.; Trichet, A. A. P.; Powell, A. W.; Taylor, R. A.; Warner, J. H.; Smith, J. M. Room-Temperature Exciton-Polaritons with Two-Dimensional WS2. *Sci Rep* **2016**, *6* (1), 33134. https://doi.org/10.1038/srep33134.

(58) Zhang, L.; Gogna, R.; Burg, W.; Tutuc, E.; Deng, H. Photonic-Crystal Exciton-Polaritons in Monolayer Semiconductors. *Nat Commun* **2018**, *9* (1), 713. https://doi.org/10.1038/s41467-018-03188-x.

(59) Ballarini, D.; De Liberato, S. Polaritonics: From Microcavities to Sub-Wavelength Confinement. *Nanophotonics* **2019**, *8* (4), 641–654. https://doi.org/10.1515/nanoph-2018-0188.